Ceramic coatings for innovative nuclear systems

Francisco García Ferré[1], Alexander Mairov[2], Matteo Vanazzi[1], Serena Bassini[3], Marco Utili[3], Mariano Tarantino[3], Luca Ceseracciu[4], Yves Serruys[5], Lucile Beck[5], Marco G. Beghi[6], Kumar Sridharan[2], Fabio Di Fonzo[1]

[1]Center for Nano Science and Technology, Istituto Italiano di Tecnologia, Italy
[2]Department of Engineering Physics, University of Wisconsin-Madison, USA
[3]ENEA-FSN-ING Division, C.R. Brasimone, Italy
[4]Smart Materials, Nanophysics, Istituto Italiano di Tecnologia, Italy
[5]Laboratoire JANNUS, DEN-Service de Recherches de Métallurgie Physique, CEA, France
[6]Dipartimento di Energia, Politecnico di Milano, Italy

Abstract

The high operating temperatures and radiation damage levels foreseen in innovative nuclear systems are expected to accelerate corrosion kinetics in most of the reactor designs. Among several corrosion mitigation strategies, ceramic coatings stand as a promising option. Here, fully dense and compact Al_2O_3 coatings are grown at room temperature by Pulsed Laser Deposition (PLD). The utility of the coatings as corrosion resistant barriers is examined through short-term exposure of coated 1515Ti plates to stagnant lead at 550°C (500 hours, 10^{-8}-10^{-9} wt.% O). Post-test analyses by SEM reveal no signs of corrosion. The effect of radiation damage on the coatings is investigated through heavy ion irradiation up to damage levels of 20, 40 and 150 displacements per atom at 600°C. TEM analyses reveal that the as-deposited coatings are mainly amorphous and contain a homogeneous dispersion of ultra-fine (6±4 nm) crystalline nano-domains. The structural evolution upon irradiation is characterized by crystallization of the amorphous phase, which is accompanied by a dramatic increase of the nanoindentation hardness. Increasing radiation damage levels induce grain growth, twinning and Hall-Petch softening. The performance of the coatings under impact loading is examined by nanoimpact tests. The impact energy is dissipated more efficiently in the irradiated samples –specifically, through localized crystalline-to-amorphous transformations. In spite of the high radiation damage levels reached, no delamination is observed at the coating-substrate interface. Overall, PLD-grown Al_2O_3 is a promising coating material for innovative nuclear systems.

Introduction

The core of Generation IV (GIV) nuclear reactors is an extremely harsh environment, where materials are called to face high temperature and radiation damage for extended periods of time. These conditions will accelerate corrosion kinetics in most of the reactor designs, opening new pathways for materials degradation [1]. The main candidate coolants for innovative nuclear reactors and fusion systems include supercritical water, helium gas, molten salts, or liquid metals like sodium, lead, lead-bismuth or lead-lithium. These coolants are usually detrimental to the reliability of structural materials. Issues such as oxidation [2] and irradiation-assisted stress corrosion cracking [3][4] are of particular concern when the coolant is supercritical water. In gas-cooled concepts, despite the fact that the coolant contains only parts per million levels of impurities (i.e. Co_2, CO, H_2, H_2O or CH_4), oxidation, oxide reduction, carburization or decarburization take place inexorably due to the rapid kinetics at the operating temperature range (i.e., approaching 1000°C) [5][6]. The major concern in the case of molten salt coolants is direct dissolution of alloying components [7][8]. Lastly, if the coolant is a liquid metal, the main corrosion mechanisms include embrittlement [9-12], oxidation [13-15], dissolution [15-19], and erosion [20][21].

A detailed knowledge of the corrosion mechanisms and rates of microstructure degradation is important to estimate the lifetime of nuclear components and define mitigation strategies. However, it is unlikely that bare alloys can maintain their integrity under GIV and fusion conditions without any protective layer [1]. The development of protective coatings that ensure the longevity of structures is, beyond doubts, one of the greatest challenges in the quest for suitable materials solutions for innovative nuclear systems. Among many possibilities, oxide coatings are an interesting option - especially for helium- or liquid metal-cooled systems, owing to the chemical compatibility of oxides with these coolants.

Recent work has highlighted that Al_2O_3 coatings grown by Pulsed Laser Deposition (PLD) are a suitable and promising solution for protecting structural steels in liquid metal environments. The coatings are known to perform flawlessly in short-term corrosion tests in high temperature lead (i.e. 550°C, 500 hours, oxygen-saturated lead, stagnant and flowing conditions) [22][23]. Further, the coatings possess an unusual ensemble of metal-like mechanical properties, ceramic hardness and strong interfacial bonding [24]. These features are important because the similarity of mechanical properties with steels avoids stress concentrations, reducing the risk of cracking or delamination. This has been confirmed by thermal cycling, thermal shock, accelerated strain and burst experiments conducted on coated 316L tubes (*unpublished data*). In this work, PLD-grown Al_2O_3 coatings are exposed to short-term corrosion tests at high temperature (550°C, 500 hours) in low-oxygen lead. In spite of the great potential as efficient corrosion barriers, one of the major challenges that coatings must face is related to structural integrity and adhesion under irradiation. The effect of radiation damage on the structural features and mechanical properties of the coatings is examined using heavy ion-irradiation as a surrogate of neutron irradiation. The damage levels attained are 20, 40 and 150 displacements per atom at 600°C.

Materials and Methods

Sample preparation

Al_2O_3 coatings are grown by PLD on 1515Ti grade steel plates (1 cm x 3 cm x 1 mm). This class of steels is currently considered as the main option for several GIV reactor designs based on heavy liquid metal coolants. The nominal composition of the steel plates is 14.9Cr-15.1Ni-1.6Mn-1.4Mo-0.8Si-0.4Ti-0.09C-balance Fe (wt. %). The preparation protocol for the steel plates includes grinding,

polishing and sonication steps. The Al_2O_3 coatings are approximately 1 µm thick. A schematic of the PLD system used for the depositions is shown in Figure 1. The depositions are performed at room temperature in a stainless steel vacuum chamber. The baseline pressure is 10^{-3} Pa. The background pressure during the depositions is 0.1 Pa oxygen. The UV (248 nm) laser pulses are focused on a 99.999% pure solid Al_2O_3 target. The energy of the laser pulses is 400 mJ, and the fluence is adjusted to a value of 3.5 J/cm^2. The pulse repetition rate is 20 Hz. The steel plates are positioned at a target-to-substrate distance of 5 cm. The sample holder is rotated during the depositions, and the resulting deposition rate is approximately 1 nm/s over an area of 25 cm^2.

Figure 1: Schematic of a Pulsed Laser Deposition system

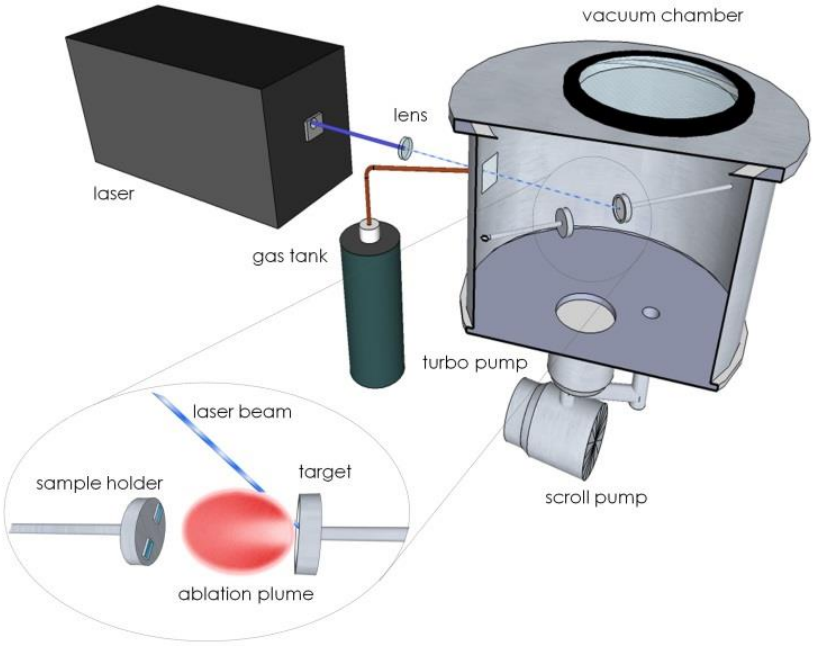

Corrosion tests

The corrosion tests are performed in stainless steel capsules. Alumina crucibles are positioned inside the steel capsules, and act as lead containers. The purity of the lead used in the tests is 99.97%. The temperature of the capsule is raised up to 550°C at 3°C/min and is held constant throughout the duration of the experiments (500 hours). The cover gas in the capsules is an Ar/H_2 mixture containing approximately 10% H_2. The oxygen content in the liquid metal is monitored with a Pt-air oxygen sensor for liquid metals, and is kept in the range 10^{-8}-10^{-9} wt.% throughout the tests. The resulting thermodynamic conditions are located below the stability range for Fe_3O_4 according to the Ellingham diagram. The samples are inserted in the crucibles once the oxygen content measured is constant, and are extracted from the crucibles after 500 hours. The samples are left to cool down at 2°C/min inside the steel capsules. Any eventual lead scale solidified on the surface of the samples is deliberately left on the surface for further analyses.

Irradiations

Three irradiations are performed with heavy ions at the JANNUS platform of Saclay [25], using double beams of 12 MeV Au^{5+} ions and 18 MeV W^{8+} ions. The ion energies are chosen to inject the ions deep into the steel substrates, avoiding chemical and interstitial injection effects in the coatings. The angle of incidence of the beams is 15°, and the irradiated area is 3.14 cm^2. According to SRIM calculations, the implantation depth of gold and tungsten ions is approximately 1.75 µm and 2.4 µm from the surface of the samples, respectively. The irradiations are carried out in vacuum (10^{-5} Pa). The irradiation temperature is monitored and kept constant at 600°C during the tests. The temperature ramps are approximately 6°C/min both during heating and cooling. The radiation damage levels attained are calculated from the ion fluences according to the recommendations by Stoller *et al.* [26]. The fluences of the three irradiations are 1.20 10^{16} $W^{8+}cm^{-2}$ + 1.74 10^{16} $Au^{5+}cm^{-2}$, 2.13 10^{16} $W^{8+}cm^{-2}$ + 2.76 10^{16} $Au^{5+}cm^{-2}$, and 4.52 10^{16} $W^{8+}cm^{-2}$ + 1.2 10^{17} $Au^{5+}cm^{-2}$. These fluences correspond to radiation damage levels similar to 20, 40 and 150 dpa within the Al_2O_3 coatings, and to peak damage levels in the 1515Ti substrates of 60, 120 and 450 dpa. The damage levels at the coating-substrate interface are given by a marked gradient between the damage levels in the coating and the peak damage levels in the steel substrate.

Characterizations

The coated steel plates are analyzed by cross-sectional Scanning Electron Microscopy (SEM) in the as-deposited condition, and after the corrosion tests. The SEM observations are performed using a JSM-6010-LV Jeol SEM. The electron voltage is set at 18 kV for imaging. The preparation of the samples is carried out following standard procedures.

Bright-Field (BF), Dark-Field (DF) and High-Resolution (HR) Transmission Electron Miscroscopy (TEM) analyses are performed using a FEI Titan (S)-TEM system. The accelerating voltage is 200 kV. TEM samples are prepared by conventional Focused Ion Beam (FIB) lift-off procedures.

The nanoindentation hardness is measured at room temperature with a Micromaterials Nanotest system. The indentations are applied with a Berkovich tip in arrays of nine indentations for each radiation damage level. The measurements are done following the usual Oliver and Pharr approach. The maximum load used is 10 mN, corresponding to penetration depths below one tenth of the thickness of the coatings.

The performance of the coatings under impact loading is investigated by nanoimpact testing. In these tests, a cube-corner diamond tip is blasted periodically against the surface of the samples with a Micromaterials Nanotest system. The tip is placed at a fixed distance from the surface of the samples (10 µm), and is blasted with a force of 1 mN through a solenoid behind the tip. The solenoid is connected to a time relay. The speed of impact is 500 µm/s. For each impact, the force is held for 3 seconds while displacement is recorded. The force is then released over the next 2 seconds. Three sets of 10 impacts are carried out after 150 dpa.

Results and Discussion

Figure 2 displays two SEM micrographs of the coated 1515Ti plates in the as-deposited condition, and after 500 hours exposure to stagnant lead at 550°C (10^{-8}-10^{-9} wt.% O). No changes are apparent in the cross-sections, but for the presence of a solidified lead scale in Figure 2b. The dark contrast zones within the lead scale are due to the SiC debris brought about during grinding. No dissolutive nor oxidation attacks are found in any of the samples tested. Thus, the Al_2O_3 coatings act as efficient corrosion-resistant barriers against heavy liquid metal corrosion.

Figure 2: Coated steel plates before (a) and after (b) 500 hours exposure to low-oxygen lead at 550°C.

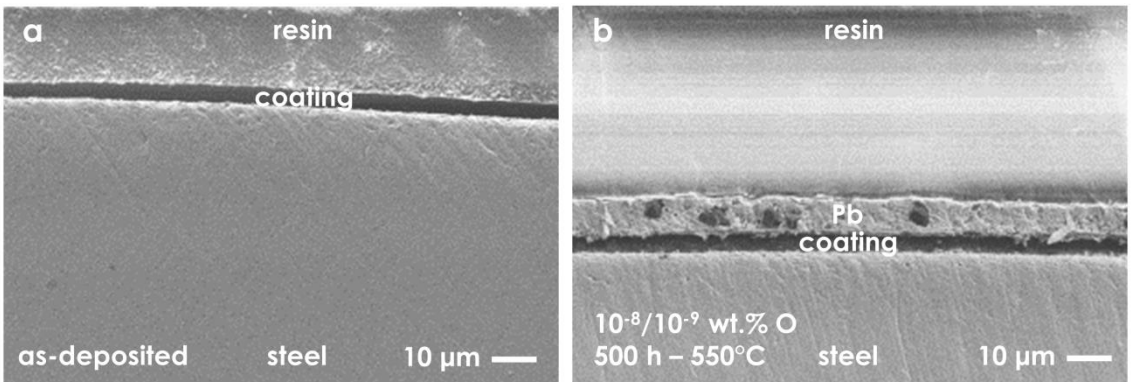

The as-deposited nanostructure of the films is shown in Figure 3. The homogeneously distributed bright contrast spots identify crystalline nano-domains. The size of these spots is approximately 6±4 nm, and the phase is γ-Al_2O_3 [27]. The dark contrast is brought about by the amorphous phase. The corresponding electron Diffraction Pattern (DP) displays diffraction rings and spots, which can be attributed to the crystalline phase, together with a diffused halo of intensity that is due to the presence of the amorphous matrix. The volume fraction of the γ-Al_2O_3 nanocrystals in the amorphous matrix is around 1% [27]. This kind of bi-phase Al_2O_3 nanocomposite is thought to be self-assembled during the particular conditions of the PLD deposition process [24].

Figure 3: DF-TEM micrograph of the as-deposited nanostructure of PLD-grown Al_2O_3 coatings.

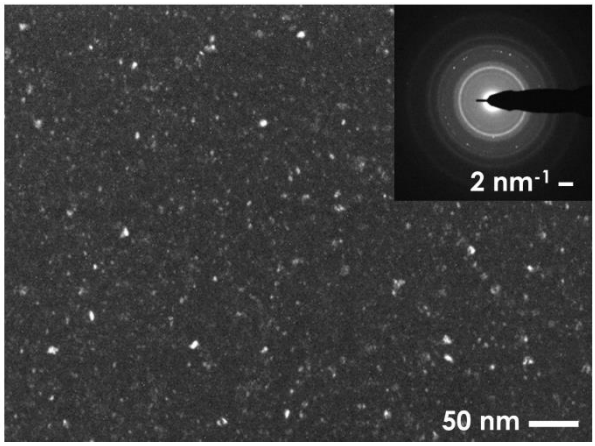

The effect of heavy ion irradiation on the as-deposited nanostructure of the coatings is shown in Figure 4. Initially, irradiation induces a transition to a fully nanocrystalline structure. As radiation damage levels increase, grain growth is observed. The coarsening effect is confirmed by the refinement of the DPs, shown as insets. The average grain size increases from 101±56 nm at 20 dpa,

to 153±62 nm at 40 dpa and 293±85 nm at 150 dpa. The initial crystallization may be either homogeneous [28], epitaxial [29], or both. The subsequent grain growth has been observed in other oxide nanoceramics, such as ceria [30], yttria-stabilized zirconia [31] or zirconia [32], and has been explained by a fast disorder-driven mechanism [32]. The phases present in the irradiated coatings are γ-Al_2O_3 up to 40 dpa, and both γ-Al_2O_3 and α-Al_2O_3 after 150 dpa [27]. It is worth noting that the irradiation spectrum (e.g., the type and energy of the incident particles) and the damage exposure have a strong influence on the final grain size and on the phase present [33]. Importantly, irradiation does not induce cracks or delamination, in spite of the very high damage levels reached.

Figure 4: BF-TEM micrographs of the nanostructure of the Al_2O_3 coatings after irradiation.

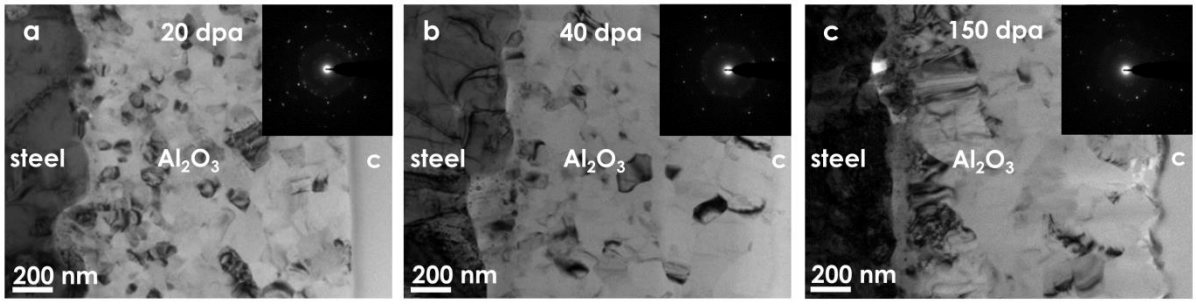

During irradiation, complex mechanical stresses may develop in the coatings due to incoherent grain growth. These stresses are released by deformation twinning, which acts as an effective energy dissipation mechanism. Twin boundaries are found in the coatings for all the damage exposures investigated, as indicated by arrows in Figure 5.

Figure 5: DF-TEM micrographs (a-d) showing twin boundaries in the Al_2O_3 coatings. The presence of a mirror plane (dashed line) in the corresponding DP (e) confirms that the boundaries are twins.

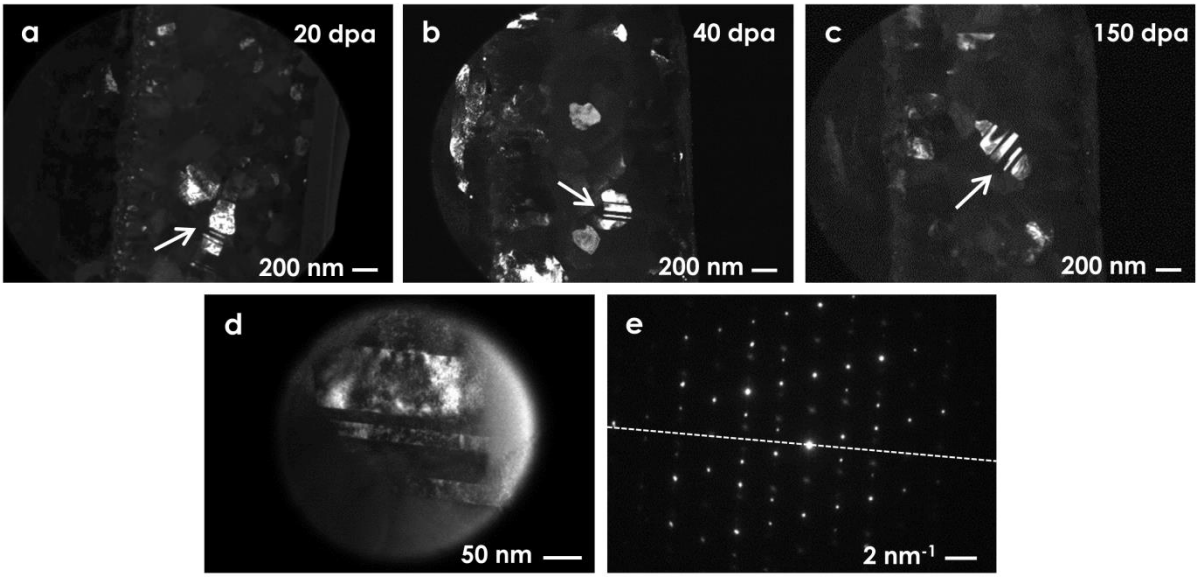

The structural rearrangements described above yield an enhancement of the hardness of the coatings. Upon crystallization, the nanoindentation hardness *H* increases dramatically from 10±1 GPa [24] to 17.8±0.9 GPa at 20 dpa. Thereafter, grain growth induces softening, and *H* decreases to 17.2±1.2 GPa at 40 dpa and 15.9±1.6 GPa at 150 dpa. The softening induced by grain growth is well fitted by the Hall-Petch relationship, as shown in Figure 6. For a grain size above a *critical grain size* (typically around 20 nm), the Hall-Petch relationship describes a decrease of hardness for increasing grain size according to the formula $H = kD^{-1/2} + H_0$, where k is the material-specific strengthening coefficient, *D* is the average grain size and H_0 is the intrinsic hardness. The improvement of hardness in the irradiated coatings suggests an enhancement of the resistance to wear, which is important in regards to liquid metal erosion or rod-to-grid fretting.

Figure 6: Trend of hardness for the irradiated Al_2O_3 coatings. The trend is well described by the Hall-Petch effect, according to which an increase of the average grain size *D* is accompanied by a decrease of the hardness *H*.

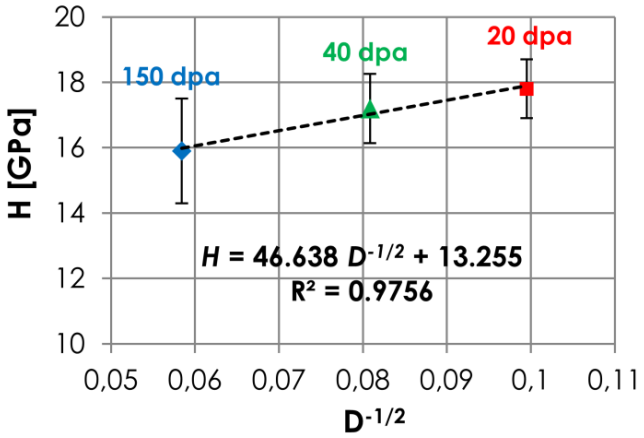

Lastly, the nanoimpact tests performed reveal that the impact depth is always higher in the irradiated coatings than in the as-deposited samples. This result suggests that the impact energy is dissipated more efficiently, and that the fracture toughness may be higher in the irradiated coatings. The results are plotted in terms of the impact depth as a function of the number of impacts in Figure 7. The impact depth tends to saturate for an increasing number of impacts because the applied force is distributed over increasing contact areas. Therefore, the contact pressure decreases for increasing number of impacts. In the as-deposited coatings, the impact energy is dissipated through shear-banding. The main energy dissipation mechanisms in the irradiated coatings are lattice plasticity and localized amorphization [25].

Figure 7: Nanoimpact curves before and after irradiation.

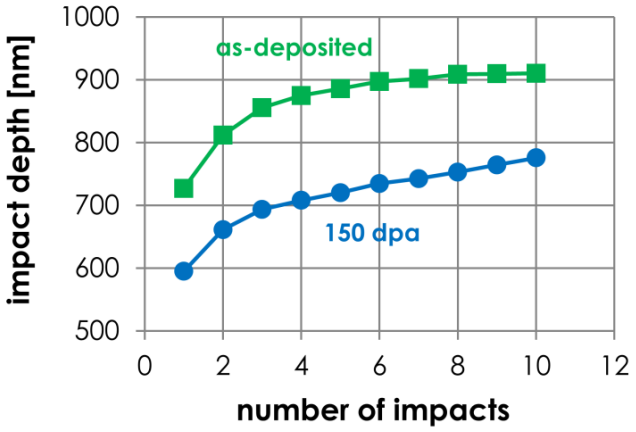

Figure 8a shows a cross-sectional BF-TEM micrograph of a typical nanoimpact imprint in the irradiated samples. The most interesting features found below the imprints are the bright contrast bands indicated by arrows. The bright contrast indicates a lower density compared to the surrounding material. The HR-TEM micrograph in Figure 8b displays an example of such bands in high-resolution. The micrograph shows that the bright contrast bands are not cracks but rather localized amorphous Al_2O_3 bands, as confirmed by the Fast Fourier Transform insets and the energy dispersive x-ray spectroscopy scans (not shown). It is worth highlighting that crystalline-to-amorphous phase transformations such as the ones found here are usually described as efficient toughening mechanisms [34]. In the present case, the transformation is likely due to the coalescence of radiation-induced defects and defect clusters under mechanical stress [25].

Figure 8: BF-TEM (a) and HR-TEM (b) micrographs revealing the presence of localized crystalline-to-amorphous transformations underneath the nanoimpact imprints in irradiated samples.

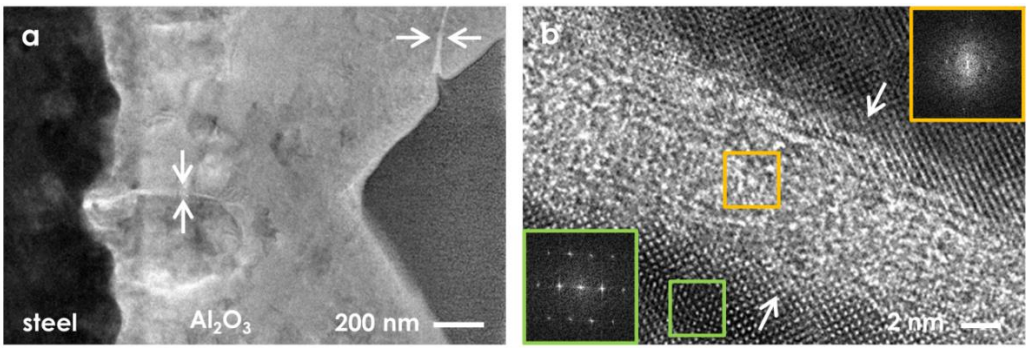

Conclusions

Overall, the results of this work encourage the use of ceramic coatings as corrosion resistant barriers in highly corrosive and high radiation environments, such as innovative nuclear systems. In particular, PLD-grown Al_2O_3 coatings are shown to perform well during short-term exposure to high-

temperature, low-oxygen static lead. The good results obtained suggest that the coatings might also perform well under different conditions (i.e., temperature, oxygen content, exposure time, flow conditions) and, perhaps, in different environments (i.e., high temperature helium or others). The outstanding radiation tolerance of PLD-grown Al_2O_3 under extreme heavy ion irradiation warrants further investigation with different types of particles. Light ion, proton and neutron irradiations are desirable to compare results and establish correlations between the outcomes of different types of irradiations.

Acknowledgements

The French network of irradiation facilities "EMIR" is acknowledged for financial support for the ion irradiations performed at the JANNUS (Joint Accelerators for Nanoscience and Nuclear Simulation) platform of CEA-Saclay, France. The authors also wish to acknowledge financial support by ENEA through AdP MiSE-ENEA project B3.1, PAR 2015.

Additional Information

This work contributes to Sub-Program 3 (SP3) of the Joint Program on Nuclear Materials (JPNM) of the European Energy Research Alliance (EERA).

References

[1] S.J. Zinkle, G.S. Was (2013), "Materials challenges in nuclear energy", *Acta Mater.*, 61, pp. 735-758.

[2] G.S. Was *et al.* (2007), "Corrosion and stress corrosion cracking in supercritical water", *J. Nucl. Mater.*, 371, pp. 176-201.

[3] R. Zhou, E.A. West, Z. Jiao, G.S. Was (2009), "Irradiation-assisted stress corrosion cracking of austenitic alloys in supercritical water", *J. Nucl. Mater.*, 395, pp. 11-22.

[4] S. Teysseyre, Z. Jiao, E.A. West, G.S. Was (2007), "Effect of irradiation on stress corrosion cracking in supercritical water", *J. Nucl. Mater.*, 371, pp. 107-117.

[5] C. Cabet, A. Terlain, P. Lett, L. Guétaz, J.M. Gentzbittel (2006), "High temperature corrosion of structural materials under gas-cooled reactor helium", *Mater. Corros. - Werkstoffe Korros.*, 57, pp. 147-153.

[6] F. Rouillard, C. Cabet, K. Wolski, M.J. Pijolat (2007), "Oxide-layer formation and stability on a nickel-base alloy in impure helium at high temperature", *Oxid. Metals*, 68, pp. 133-148.

[7] L.C. Olson, J.W. Ambrosek, K. Sridharan, M.H. Anderson, T.R. Allen (2009), "Materials corrosion in molten LiF-NaF-KF salt", *J. Fluorine Chem.*, 130, pp. 67-73.

[8] M. Hofmeister *et al.* (2015), "Corrosion behavior of stainless steels and a single crystal superalloy in a ternary LiCl-KCl-CsCl molten salt", *Corros. Sci.*, 90, pp. 46-53.

[9] S. Hémery, T. Auger, J.L. Courouau, F. Balbaud-Célérier (2013), "Effect of oxygen on liquid sodium embrittlement of T91 martensitic steel", *Corros. Sci.*, 76, pp- 441-452.

[10] S. Hémery, T. Auger, J.L. Courouau, F. Balbaud-Célérier (2014), "Liquid metal embrittlement of an austenitic stainless steel in liquid sodium", *Corros. Sci.*, 83, pp. 1-5.

[11] G. Coen, J. Van den Bosch, A. Almazouzi, J. Degrieck (2010), "Investigation of the effect of lead-bismuth eutectic on the fracture properties of T91 and 316L", *J. Nucl. Mater.* 398, pp. 122-128.

[12] J. Van den Bosch, G. Coen, P. Hosemann, S.A. Maloy (2012), "On the LME susceptibility of Si enriched steels", *J. Nucl. Mater.*, 429, pp. 105-112.

[13] L. Martinelli *et al* (2008), "Oxidation mechanisms of a 9Cr-1Mo steel by liquid Pb-Bi eutectic alloy. Part I.", *Corros. Sci.*, 50, pp. 2523-2536.

[14] P. Hosemann, R. Dickerson, P. Dickerson, N. Li, S.A. Maloy (2013), "Transmission electron microscopy (TEM) on oxide layers formed on D9 stainless steel in lead bismuth eutectic (LBE)", *Corros. Sci.*, 66, pp. 196-202.

[15] I.V. Gorynin, G.P. Karzov, V.G: Markov, V.S. Lavrukhin, V.A. Yakovlev (1999), "Structural materials for atomic reactors with liquid metal heat transfer agents in the form of lead or lead-bismuth alloy", *Met. Sci. Heat Treat.,* 41, pp. 384-388.

[16] T. Suzuki, I. Mutoh, T. Yagi, Y. Ikenaga, Y (1986), "Sodium corrosion behavior of austenitic alloys and selective dissolution of chromium and nickel", *J. Nucl. Mater.*, 139, pp. 97-105.

[17] E. Yamaki, K. Ginestar, L. Martinelli (2011), "Dissolution mechanism of 316L in lead bismuth eutectic at 500 °C", *Corros. Sci.*, 53, pp. 3075-3085.

[18] C. Schroer, O. Wedemeyer, J. Novotny, A. Skrypnik, J. Konys (2014), "Selective leaching of nickel and chromium from type 316L austenitic steel in oxygen-containing lead-bismuth eutectic (LBE)", *Corros. Sci.*, 84, pp. 113-124.

[19] G. Müller, G. *et al.* (2004), "Behavior of steels in flowing liquid PbBi eutectic alloy at 420-600 °C after 4000-7200 h", *J. Nucl. Mater.*, 335, pp. 163-168.

[20] G. Müller *et al.* (2002), "Results of steel corrosion tests in flowing liquid Pb/Bi at 420-600 °C after 2000 hours", *J. Nucl. Mater.*, 301, pp. 40-46.

[21] M. Kondo *et al.* (2005), "Metallurgical study on erosion and corrosion behaviors of steels exposed to liquid lead-bismuth flow", *J. Nucl. Mater.*, 343, pp. 349-359.

[22] F. García Ferré, M. Ormellese, F. Di Fonzo, M.G. Beghi (2013), "Advanced Al_2O_3 coatings for high temperature operation of steels in heavy liquid metals: a preliminary study", *Corros. Sci.*, 77, pp. 375-378.

[23] F. García Ferré *et al.* (2016), "Radiation tolerant nanoceramic coatings for lead-cooled nuclear systems", *submitted*.

[24] F. García Ferré *et al.* (2013), "The mechanical properties of a nanocrystalline Al_2O_3/a-Al_2O_3 composite coating measured by nanoindentation and Brillouin spectroscopy", *Acta Mater.*, 61, pp. 2662-2670.

[25] F. García Ferré *et al.* (2016), "Radiation endurance in Al_2O_3 nanoceramics", *Sci. Rep., accepted.*

[26] L. Beck *et al.* (2015), "Ion irradiation and radiation effect characterization at the JANNUS-Saclay triple beam facility", *J. Mater. Res.*, 30, pp. 1183-1194.

[27] R.E. Stoller *et al.* (2013), "On the use of SRIM for computing radiation damage exposure", *Nucl. Instr. Meth. Phys. Res. B*, 310, pp. 75-80.

[28] R. Nakamura, M. Ishimaru, H. Yasuda, H. Nakajima (2013), "Atomic rearrangements in amorphous Al_2O_3 under electron-beam irradiation", *J. Appl. Phys.*, 113, pp. 064312.

[29] Y. Sina, M. Ishimaru, C.J. McHargue, E. Alves, K.E. Sickafus (2014), "Ion beam induced epitaxial crystallization of α-Al2O3 at room temperature", *Nucl. Instr. Meth. Phys. Res. B*, 321, pp. 8-13.

[30] P.D. Edmondson, Y. Zhang, S. Moll, F. Namavar, W.J. Weber (2012), "Irradiation effects on microstructure change in nanocrystalline ceria – Phase, lattice stress, grain size and boundaries", *Acta Mater.*, 60, pp. 5408-5416.

[31] S. Dey *et al.* (2015), "Radiation tolerance of nanocrystalline ceramics: insights from Yttria Stabilized Zirconia", *Sci. Rep.*, 5, pp. 7746.

[32] D.S. Aidhy, Y. Zhang, W.J. Weber (2014), "A fast grain-growth mechanism revealed in nanocrystalline ceramic oxides", *Scripta Mater.*, 83, pp. 9-12.

[33] F. García Ferré *et al.* (2016), "Extreme ion irradiation of oxide nanoceramic coatings: the influence of the irradiation spectrum", *submitted*.

[34] M.E. Launey, R.O. Ritchie (2009), "On the fracture toughness of advanced materials", *Adv. Mater.*, 21, pp. 2103-2110.